A Unit-Problem Investigation of Blunt Leading-Edge Separation Motivated by AVT-161 SACCON Research

James M. Luckring

NASA Langley Research Center, Hampton VA, 23681, USA

James.m.luckring@nasa.gov

Okko J. Boelens

National Aerospace Laboratory NLR, Anthony Fokkerweg 2, 1059 CM Amsterdam, NLD

Boelens@nlr.nl

ABSTRACT

A research effort has been initiated to examine in more detail some of the challenging flow fields discovered from analysis of the SACCON configuration aerodynamics. This particular effort is oriented toward a diamond wing investigation specifically designed to isolate blunt leading-edge separation phenomena relevant to the SACCON investigations of the present workshop. The approach taken to design this new effort is reviewed along with the current status of the program.

1.0   NOMENCLATURE

AR	aspect ratio
b/2	semispan
C_L	lift coefficient
C_p	pressure coefficient
c	wing chord
c_r	root chord
h	peniche stand-off height
M	Mach number
t	airfoil maximum thickness
Re	Reynolds number, based upon reference chord
R_{mac}	Reynolds number, based upon mean aerodynamic chord
R_x	Reynolds number, based upon local length
r_{le}	streamwise leading-edge radius
s	local semispan
u, v, w	body-axis velocity components
V_{oo}	free stream velocity
x, y, z	body-axis Cartesian coordinate system
α	angle of attack, degrees
η	fraction of local semispan, y/s
Λ_{le}	leading-edge sweep, degrees
Λ_{te}	trailing-edge sweep, degrees

Acronyms:

ASME   American Society of Mechanical Engineers
AVT   Applied Vehicle Technology
EADS   European Aeronautic Defence and Space Company
RTO   Research and Technology Organization
SACCON Stability And Control CONfiguration
UCAV   Uninhabited Combat Air Vehicle

2.0   INTRODUCTION

Smooth surface separation continues to be challenging flow phenomena that can affect many vehicle classes. For military vehicles with high-speed capability, one such phenomenon is the leading-edge vortex separation that forms at moderate-to-high angles of attack. While much is known about this class of separated flow for slender wings with sharp leading edges, practical vehicle design considerations often result in blunt leading edges with lower leading-edge sweep values than the traditional slender wing. These wings are still conducive to leading-edge vortex separation, although the details are greatly complicated by the leading edge bluntness and reduced sweep, and much less is known about this class of vortical separation. A recent survey of some factors affecting blunt leading-edge separation has been developed by Luckring[1] [2010].

One class of aircraft where this separation can be important are the Uninhabited Air Combat Vehicles, or UCAVs, that incorporate capability for high subsonic or transonic flight. Several examples of full aircraft (i.e., completely integrated systems) are shown in **Figure 1** that also illustrate distinctions among current wing design concepts. The X-45A represents a lambda wing concept that incorporates an outboard constant chord section with the inner fuselage. The X-45C represents a more blended wing-body concept and also incorporates a swept and tapered wing. Finally the X-47A represents a slender-wing concept with yet more blended diamond wing-body geometry. All of these concepts incorporate moderate leading-edge sweep values and small leading-edge radii. Both the moderate sweep and blunt leading edge can significantly alter the separation-induced leading-edge vortical flows from those that occur on slender sharp-edged wings.

A significant contribution pertinent to UCAV configuration aerodynamics has been recently completed by the RTO Task Group AVT-161, entitled "Assessment of Stability

a) X-45A, $\Lambda_{le} = 45^{o}$.

b) X-45C, $\Lambda_{le} = 55^{o}$.

c) X-47A, $\Lambda_{le} = 55^{o}$.

**Figure 1. UCAV aircraft concepts.**

and Control Prediction Methods for NATO Air & Sea Vehicles" and is the focus on the present specialists meeting. This work is of course focused on the UCAV configuration known as SACCON (Stability And Control CONfiguration), see **Figure 2**, and the project orientation to stability and control includes both static and dynamic conditions, with a considerable (perhaps primary) effort directed toward obtaining dynamic data and dynamic CFD simulations for the vehicle interests. However, to do the dynamic studies requires baseline information to also be obtained for static conditions. An overview of the SACCON work has recently been given by Cummings and Schütte[2] [2010].

Among the contributions from the SACCON research has been the identification of remaining challenges and limitations of current CFD methods for the prediction of UCAV configuration aerodynamics. A representative example is shown in **Figure 3** for static pitching moment predictions from Frink[3] [2011]. Frink's results as well as analyses by Schütte[4] [2010] and others have demonstrated that multiple vortex flow phenomena (e.g., blunt-edge vortex onset and progression, vortex-vortex interactions, vortex breakdown, etc.) are occurring on the SACCON configuration especially in the moderate-to-high angle of attack region where the scatter among CFD results is large.

Figure 2. Stability And Control CONfiguration (SACCON).
$\Lambda_{le} = 53^o$.

Advancements to our knowledge of complex flow phenomena pertinent to practical configurations can benefit from investigations at differing representation levels of vehicular and flow complexity. These investigation levels span from assessments of the complete vehicular system at intended operating conditions to fundamental unit-problem or perhaps validation studies. It has been demonstrated by Thacker[5] [2008] among others that roughly four representation levels can suffice to span this notional domain from fundamental studies to complete system assessments. It is, of course, important that the investigations among these various levels of configuration and/or flow representation be carefully coupled for relevancy.
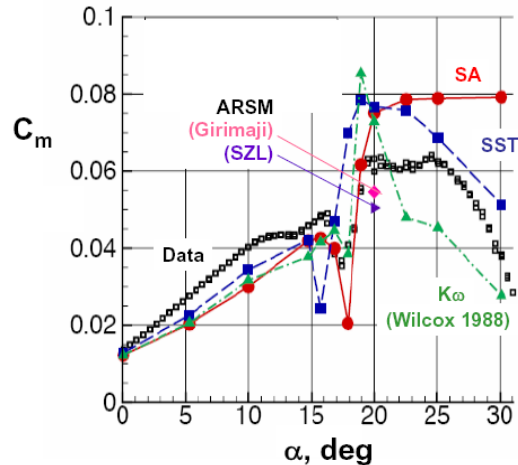
Figure 3. RANS pitching moment predictions.
USM3D, M = 0.14, Re = 1.6 x 10^6. Frink [2011].

This paper addresses a current research effort recently initiated under the RTO Task Group AVT-183, entitled "Reliable Prediction of Separated Flow Onset and Progression for Air and Sea Vehicles". This particular effort is oriented toward a diamond wing investigation specifically spawned from aggregated findings of the AVT-161 UCAV SACCON investigations of the present workshop. In this regard, AVT-161 is a sponsoring research activity, at a higher level of system complexity, for the relevant but more fundamental diamond wing

investigations of AVT-183.

The organization is as follows. First, some fundamental vortex flow phenomena are briefly reviewed. Each of these phenomena still has unique challenges, not only as regards our understanding of underlying fundamentals and flow physics, but also as regards their manifestation on complex vehicle systems. There is of course interest in improved modelling of vortex phenomenology pertinent to configuration aerodynamics, and the next section of the paper highlights some of the evolving concepts for code discrimination research that relate to this interest. Finally, the evolution, approach, and status for the new AVT-183 work are summarized. Some concluding remarks are also provided.

3.0   VORTEX FLOW PHENOMENA

There are a suite of vortex flow phenomena, each with underlying flow physics, to be considered in addressing any manifestation of separation-induced vortex flows to configuration aerodynamics. To some degree these can occur in isolation, although some are inherently coupled. These phenomena can be reviewed following slender-wing principles. Some comments regarding lower-sweep or semi-slender wing effects will follow.

3.1   Slender wing, sharp edge

3.1.1   Primary and secondary vortices

Here some basic attributes of separation-induced leading-edge vortex flows are reviewed for slender sharp-edged delta wing. At essentially any non-zero angle of attack separation is forced to occur at the sharp leading edge and for the slender wing this separation rolls up to form a stable primary leading-edge vortex. A sketch, due to Hummel[6] [1979], is shown in **Figure 4** that illustrates this primary leading-edge vortex.

The primary vortex induces significant spanwise flow on the wing upper surface resulting in the negative suction peak also illustrated in Hummel's sketch. Past the primary suction peak the adverse spanwise pressure gradient induces separation of the spanwise boundary layer flow resulting in a secondary separation and secondary vortex. The secondary vortex is counter rotating with respect to the primary vortex and can induce further suction outboard of the primary vortex suction peak. The primary and secondary vortices are tightly coupled, and factors affecting the secondary vortex (e.g., if the secondary separation is laminar or turbulent) also affect the primary vortex.
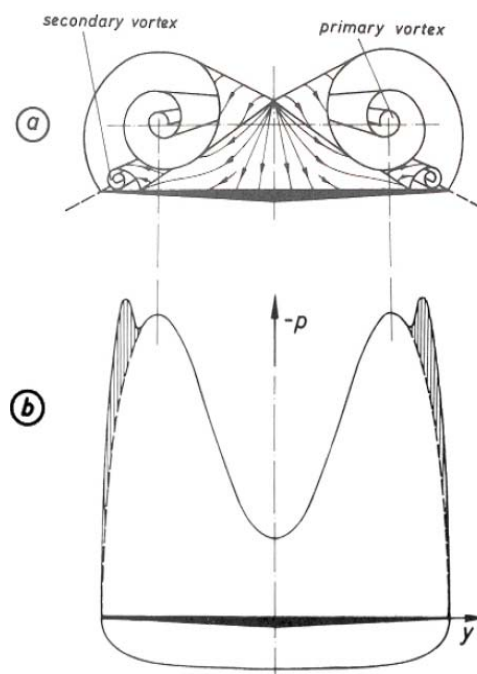

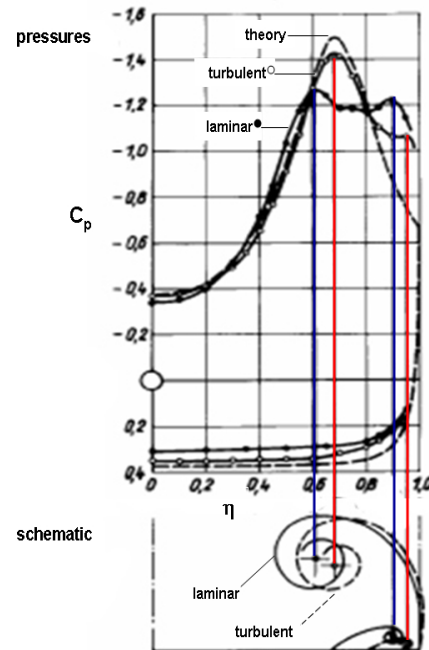**Figure 4. Primary and secondary vortex structures. Hummel [1979].**

An example of this coupling is shown in **Figure 5** from Hummel[7] [2004] with slight labelling modifications. Experiments were performed to alter the extent of secondary vortex separation. Data were first obtained at Reynolds numbers for which the secondary vortex separation was laminar. Through the use of a trip wire, a second set of data were obtained for which the secondary vortex separation was turbulent. Compared to the laminar case, the turbulent secondary separation is further outboard and the secondary vortex is smaller.

The effects of the secondary vortex separation on the overall flow field are shown in Figure 5. When the secondary vortex was diminished, the primary vortex moved outboard and its suction peak increased. The figure also shows the inviscid conical flow theoretical result from Smith[8] [1966]. The turbulent flow case, with reduced secondary vortex effects, seems to be approaching this theoretical estimate where there is no secondary vortex.
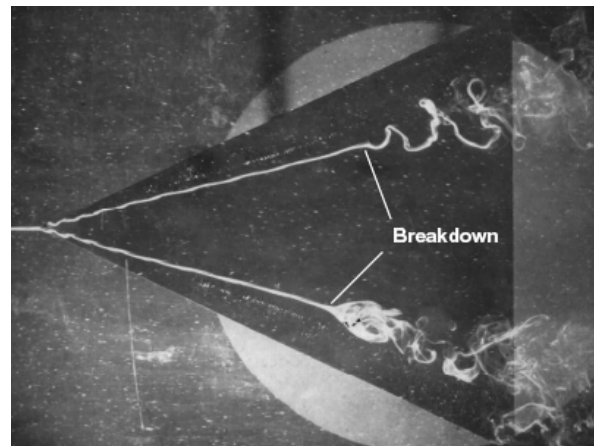
Reynolds number can be important to these flows at conventional wind tunnel values as regards the secondary separation effects. At higher Reynolds number values, where secondary separation is fully turbulent, Reynolds number effects are diminished for the sharp-edged wing. Some details can be found in the paper by Hummel[7] [2004].

Figure 5. Secondary vortex effect on primary vortex. AR = 1, α = 20.5^o, x/c$_r$ = 0.3. After Hummel [2004].

3.1.2   Vortex breakdown

The discussions thus far have addressed coherent leading edge vortices. As angle of attack increases, the leading-edge vortex gains strength until, at some angle, the vortex becomes incoherent, or bursts, in the vicinity of the wing trailing edge. With further increases in angle of attack the burst point progresses upstream, over the wing, with significant effects on wing aerodynamic characteristics such as lift, pitching moment, and buffet, to name a few. An example is shown in **Figure 6** from the well known results of Lambourne and Bryer[9] [1962]. The results show vortex breakdown in the vicinity of mid chord over a 65° flat delta wing with a sharp leading edge and illustrate two modes of breakdown; a nearly axisymmetric

Figure 6. Vortex breakdown. Λ_{le} = 65°. Lambourne and Bryer [1962].

breakdown on the port semispan and a helical breakdown on the starboard semispan. Little effect of Reynolds number on vortex breakdown characteristics for slender sharp-edged wings has been shown. Vortex breakdown, and the tantamount burst vortex flow physics, represents another class of vortex flows which is to this day insufficiently understood. Measurements in the vicinity of breakdown are very difficult to perform, the relationship of current turbulence models to the (unmeasured) breakdown flow physics is uncertain, and in many wing/vehicular applications the region of vortex breakdown is often under resolved by the field grids. A recent status of data sets and CFD predictions pertinent to vortex breakdown on slender delta wings was reported[10] in 2009 by RTO Task Group 080, entitled "Vortex Breakdown over Slender Delta Wings". Eight experimental cases were catalogued, and ten CFD approaches were included with a particular focus on a 70-degree sharp-edged delta wing experiment performed by Mitchell[11] [2003].

3.1.3 Primary vortex interactions

The coexistence of the primary and secondary vortices described above is one example of interacting vortical flows. In that case the two vortices are counter rotating, the secondary vortex is smaller and weaker than its parent primary vortex, and the two vortices tend to stay in the relationship as described.
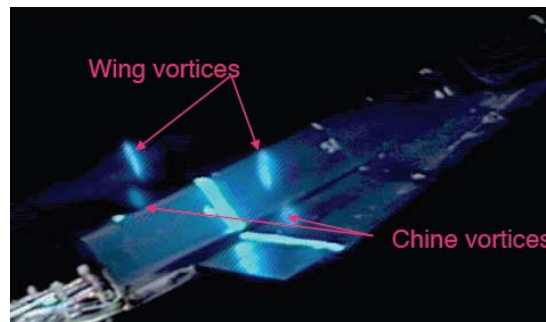
A second class of vortex interactions comes about between primary vortices that are corotating. For wings with sharp edges, such vortex flows can arise from changes in leading-edge sweep. One wing shape used to generate such vortex interactions is the double delta wing with a sharp sweep discontinuity. More recently these vortical interactions have become of interest in association with a chined forebody interacting with a semi-slender wing. An example from a basic research configuration generating these flows is shown in **Figure 7** from the work of Hall[12] [1998]. This model was known as the Modular Transonic Vortex Interaction (MTVI) configuration and incorporated several sharp-edged forebodies with sharp-edged, swept and tapered wing ($\Lambda_{le} = 60^o$).

Whereas the counter rotating primary/secondary vortex flows tend to take on a single state, corotating vortices can take on several states depending upon the relative strength and proximity of the vortices. At low angles of attack the vortices can each track somewhat independently over the body and wing, but as angle of attack increases the vortices become stronger and closer situated to each other. The induced effects will certainly alter the vortices (as compared to isolated vortex characteristics). Moreover, at some

a) MTVI configuration.

b) Interacting vortical flows.
M = 0.4, $R_{mac} = 2.6 \times 10^6$, $\alpha = 22.5^o$.

**Figure 7. Corotating leading-edge vortices.
Hall [1998].**

critical angle of attack the strong interactions between the vortices can result in the outer vortex lifting off the wing surface and braiding around the inner vortex while the inner vortex is mutually induced outboard over the wing. An example of this interaction is shown in part b of Figure 7 at a station slightly ahead of the wing

trailing edge. Here the vortex interaction has displaced the wing leading-edge vortex upward and inboard of the chine vortex which has been displaced outboard over the wing. Needless to say, vortex breakdown characteristics can be significantly altered by such vortex interactions.

Finally, it is noted that each of the primary leading-edge vortices of necessity has its own secondary vortex as described in section 3.1.1. Once again, secondary separation affects the primary vortex strength and location, and hence secondary separation would affect the interaction between the corotating primary vortices.

3.1.4 Shock-vortex interactions

Although shock waves constitute a separate class of flow structures, it would be remiss not to briefly address shock-vortex interactions. At transonic speeds the presence of shocks will fundamentally alter any vortex properties also present, and one example from Schiavetta[13] [2009] is shown in **Figure 8**. Computational results are shown for a 65° delta wing with a sharp leading edge at two angles of attack, and for both cases a shock wave has established roughly normal to the wing upper surface and the free stream direction.

The shock can be inferred from the rapid loss longitudinally of vortex suction. At the lower angle of attack the shock is located at about 80 percent chord and is associated with trailing-edge compression. At the higher angle of attack the shock is situated around 60 percent chord and is associated with the sting fairing on the wing. This shock was also shown to have spanwise curvature over the wing.

As the leading-edge vortex penetrates the shock vortex breakdown is induced. Longitudinal deceleration from the shock would contribute to inducing vortex breakdown within the vortex core, although other effects such as entropy production from the shock would further alter the flow.

Fundamental shock-vortex interactions are not limited to transonic speeds, and a number of supersonic shock-vortex interaction domains have been established by Miller and Wood[14] [1985], expanding the earlier work of Stanbrook and Squire[15] [1964]. An example from one domain is

Figure 8. Transonic example. $\Lambda_{le} = 65^o$, $M = 0.85$, $R_{mac} = 6 \times 10^6$. **Schiavetta [2009].**
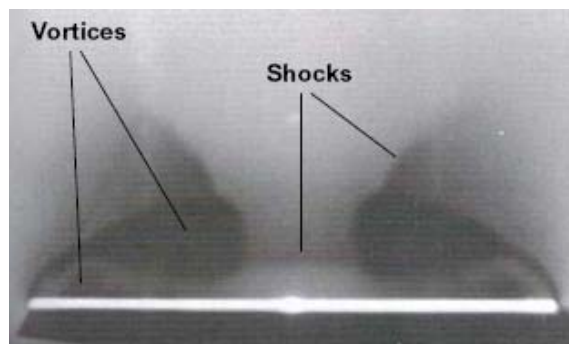
Figure 9. Supersonic shock-vortex interactions. $\Lambda_{le} = 75^o$, $M = 2.4$, $R_{mac} = 2.5 \times 10^6$, $\alpha = 20^o$. **Miller and Wood [1985].**

shown in **Figure 9**. The image is a full-span cross-flow plane vapour screen as seen looking upstream from position aft and above a 75° swept sharp-edged delta wing. In addition to the leading-edge vortices, a curved cross-flow shock can be seen atop of each vortex. There is also a shock spanning the two vortices, slightly above the wing. Six different supersonic domains distinguishing shocks, vortices, and shock-vortex interactions were identified by Miller and Wood in terms of the Mach number and angle of attack normal to the delta wing leading edge sweep. The underlying shock-vortex flow physics could differ among these domains.

3.2   Slender wing, blunt edge

All of the vortex phenomena discussed thus far are fundamentally altered by changing the leading edge from sharp to blunt. A sketch from Luckring[16] [2004] is shown in **Figure 10** to illustrate this point for the relatively simple delta wing. The left semispan illustrates a sharp leading-edge vortex with a summary of some of the vortex flow attributes discussed above. The right semispan illustrates the effect of bluntness at a moderate angle of attack. Here the origin of the leading-edge vortex is displaced from the apex of the delta wing. At low angles of attack the flow can be fully attached, and as angle of attack increases the origin of vortex separation will first occur at the wing tip and then progress up the leading edge as angle of attack is increased. In the vicinity of separation onset the separation will most likely occur slightly on the upper surface near the leading edge where pressure gradients become adverse. Although the vortex origin is shown as a point, the actual incipient separation process would be expected
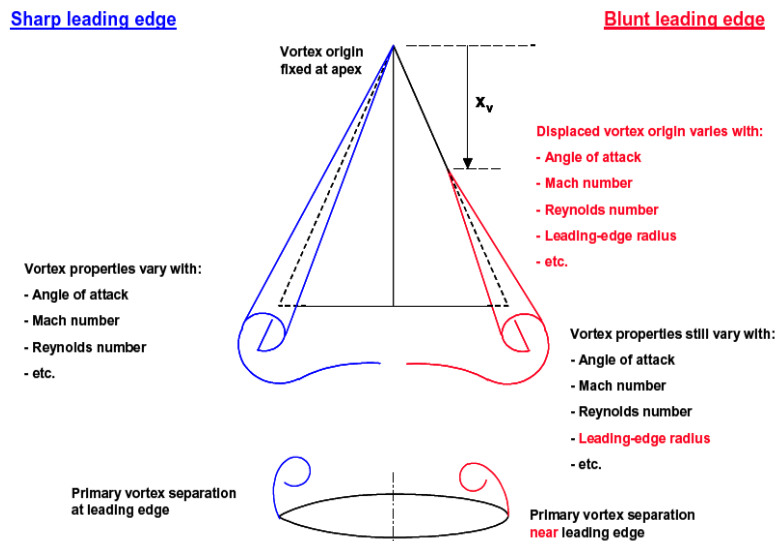
Figure 10. Sharp and blunt leading-edge separation sketch. Luckring [2004].
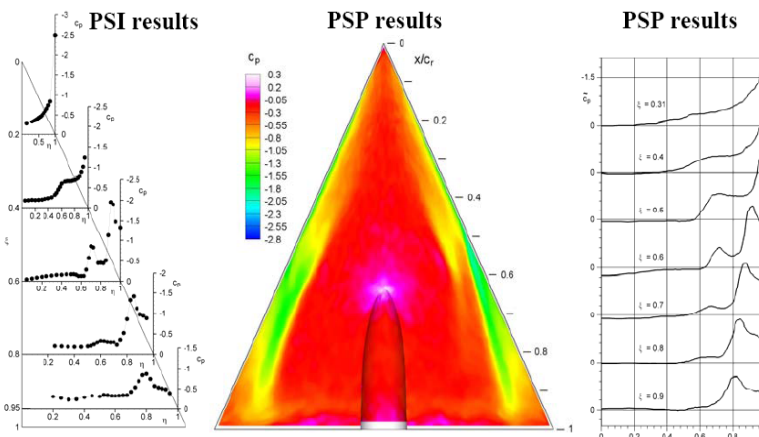
Figure 11. Blunt leading-edge part-span vortex separation.
$\Lambda_{le} = 65°$, $M = 0.4$, $R_{mac} = 3 \times 10^6$, $\alpha = 13°$. Konrath [2008].

to be drawn out over some region and affected by flow details slightly upstream of this location. Some recent results from Konrath[17] [2008] are shown in **Figure 11**. In this figure pressure orifice measurements (PSI) and pressure paint measurements (PSP) from tests at DLR clearly show the part span vortex separation. The full-span pressure paint results show a similar separation onset location for both semispans although some details differ on each side. These differences could be could be associated with small differences in model geometry.

All the previously discussed vortex phenomena are modulated by the blunt leading-edge separation. First, the vortex is smaller and situated further outboard with a part-span blunt leading separation than would be the case for the sharp edge resulting in an altered flow field within which the leading-edge vortex self establishes. Next, the blunt-edge separation slightly beyond the leading edge will weaken the vortex with possible consequences to vortex breakdown. In addition, shifts in load distributions associated with the part-span vortex separation contribute induced effects that further alter the part-span vortex from the more familiar sharp-edged full-span case. Finally, Reynolds number has significant effects on these flows as regards the blunt leading edge separation as discussed by Luckring[16] [2004]. An increase in Reynolds number will delay the onset and progression of the blunt leading-edge separation. In the same work Luckring shows that an increase in Mach number will promote this separation. These Mach and Reynolds number effects are absent for the sharp-edged wing.

As is the case with the SACCON configuration, variations in leading-edge radius can be a source of multiple primary corotating leading-edge vortices. The bluntness further affects the location of the vortices and hence modulates any vortex interaction phenomenology. At higher speeds, the bluntness and part-span vortex flow would fundamentally alter the presence and location of shocks resulting in altered shock-vortex interaction effects.

3.3 Semi-slender wing

The above examples have been purposely anchored within slender-wing aerodynamics. The high sweep angles are conducive to the formation and subsequent study of separation-induced leading-edge vortex flows. This class of wing still affords many opportunities to advance our understanding of these vortex flows.

Practical wing design considerations however result in lower leading-edge sweep values and higher aspect ratios than the more traditional slender-wing. The examples shown in Figure 1 have leading-edge sweep angles between 45° and 55° and moderate aspect ratios. Such wings can be referred to as semi-slender wings. The semi-slender wing is very challenging for wing design and analysis in that it can be unclear the extent to which either slender-wing or high aspect-ratio-wing principles apply.

From the slender wing perspective, two effects are noteworthy. First, as sweep is decreased, the leading-edge vortex strength will increase. (See Hemsch and Luckring[18]). Among other consequences, this means that vortex breakdown will occur at lower angles of attack, in association with the lower sweep, and thus potentially impact more of the practical angle of attack range. Second, the trajectory of the leading-edge vortex is at a greater angle to the free stream direction for the semi-slender wing. This can increase spanwise vortex curvature over the wing (departing from slender wing aerodynamics) and potentially entice multiple spanwise vortex structures. Much less is known about the separation-induced leading-edge vortices for these semi-slender wings than for the more highly swept slender wing.

4.0   CODE DISCRIMINATION MOTIVATED RESEARCH

In this section several factors useful to code-discrimination research are briefly reviewed. These can help establish the understanding of complex vehicle aerodynamics through the study of reduced complexity problems that are none the less relevant to the more complex vehicle aerodynamics of interest. Topics included i) problem hierarchy, ii) verification and validation, and iii) uncertainty. These can be useful toward developing improved code prediction capabilities. Code-discrimination research differs slightly from code-validation research. Code discrimination work has an orientation simply to discriminate why codes and models match or miss aerodynamics of interest from an underlying flow physics perspective; code-validation research is oriented toward validating a particular model.

4.1 Hierarchical Approach

The establishment of a problem complexity hierarchy is certainly not new and for this work we draw upon the recent publication by Thacker[5] [2008] as well as the ASME verification and validation Guide[19] [2008]. An example in terms of the current research interests of this paper is shown in **Figure 12**. The hierarchy of complexity decomposition spans from full aircraft assessments to fundamental/unit investigations. As the level system complexity is reduced, underlying flow physics tend to be isolated.
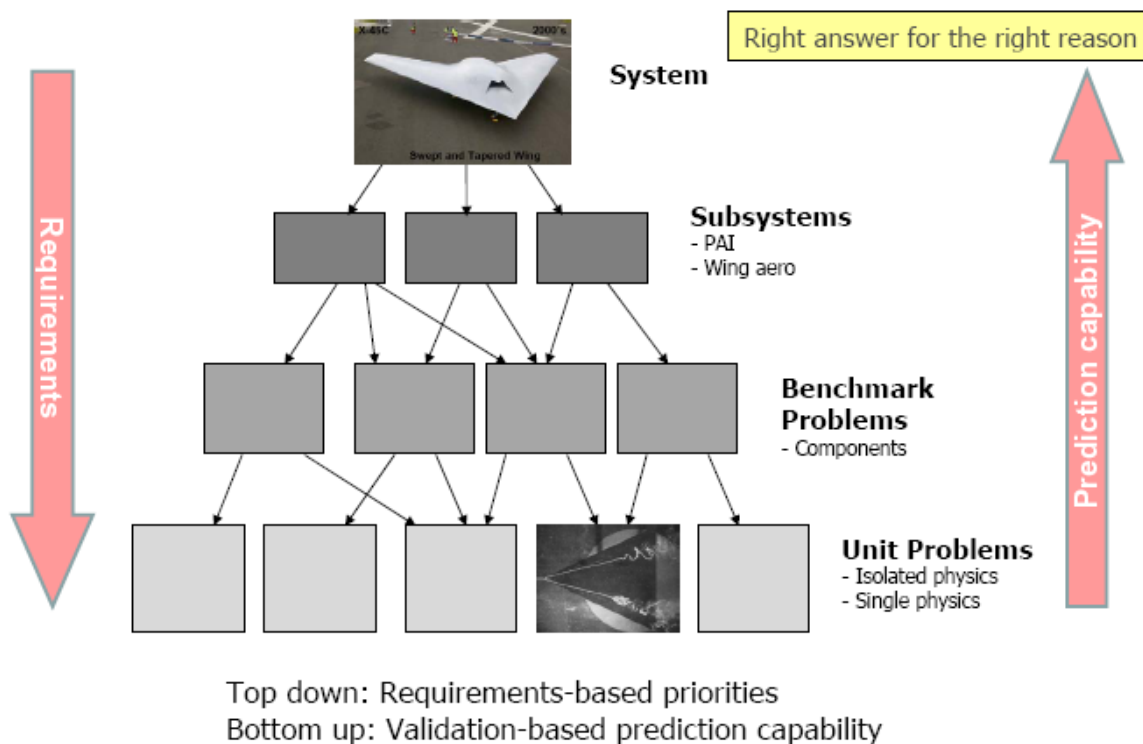
Figure 12. Hierarchy of system decomposition.

At the highest tier, the aircraft configuration aerodynamics can be complex due to (i) interaction effects among subsystems (e.g., propulsion-induced effects on wing aerodynamics), (ii) interactions among more fundamental aerodynamic flow phenomena (e.g., shocks and vortices), (iii) full system geometric

complexities, and (iv) full system operating conditions (e.g, flight Reynolds numbers). Full systems-level assessments tend to be better at explaining what the performance is than at explaining why the performance is as it is.

At the lowest tier the situation is somewhat reversed. Fundamental/unit problems are, by their very nature, designed to isolate, as best possible, a single aerodynamic phenomenon and understand why results occur as they do. However, the understanding of what the fundamental results mean to systems level performance can be more difficult. Thus, the lower levels tend to be conducive to code-validation research whereas the higher levels are conducive to configuration aerodynamics assessments.

The hierarchical approach provides a rational means for bridging this gap. Requirements flow down the hierarchy. That is, problems are identified and priorities are established from the Systems level, and are used to inform the lower levels in such a way help select the more basic work done at benchmark/unit levels of complexity. This flow down of priorities can be done heuristically or with more formal methods such as a Phenomena Identification and Ranking Table (PIRT) as reported by Wilson[20] [1998]. The basic work then can help understand key flow features in a way that is relevant to higher program needs. Improved modelling then propagates up the hierarchy. This flow up can now be anchored in validation-based principles and perhaps draw on sensitivity analyses to result in better informed predictions at the higher levels. Four complexity levels can often suffice (although the exact number is not important) and naming conventions tend vary some among applications.

In terms of the present configurations of interest, the X45-C has been chosen to illustrate a full system level of configuration development. The SACCON configuration was designed by EADS and DLR to capture many aspects of UCAV concepts while at the same time purposely omitting some details (e.g., there is no inlet or propulsion related effects) to simplify the configuration and also to be suitable for international collaborative research. As such, SACCON could be considered a 'subsystem' within complexity hierarchy just discussed. At lower hierarchical levels the investigations are crafted more to isolate one component of the coupled flow physics from the full system in such a way that increased understanding of said physics can be achieved through focused experimental and numeral investigations. It is also noted that although the lower-level work will be relevant to higher-level systems, the lower-level shapes will not necessarily resemble the full system design and, similarly, the lower level investigation conditions will relate but not necessarily replicate full system operating conditions.

4.2 Verification and Validation

A considerable body of literature has been developed over the last fifteen years or so regarding the fundamental tenets of verification and validation. After considerable debate, a fairly mature theoretical perspective toward verification and validation has emerged. Useful guides have been developed by the AIAA[21] and the ASME[19, 22], and further insights can be gained from the Progress in Aerospace Sciences article by Oberkampf and Trucano[23] [2002] as well as the recent book by Oberkampf and Roy[24] [2010]. The many details from the verification and validation literature base are beyond the scope of the present paper, but a few comments pertinent to the current work are warranted.

As the understanding of verification and validation has become fairly mature, the resultant definitions found among the cited guides are very similar. Here the definitions from the ASME guide[19] [2006] are provided below:

verification: The process of determining that a computational model accurately represents the

underlying mathematical model and its solution.

validation: The process of determining the degree to which a model is an accurate representation of the real world from the perspective of the intended uses of the model.

Verification addresses whether the code is correctly written and verification assessments address the numerics of the code. Among the assessments would be studies of iterative convergence, studies of grid convergence, and comparisons against analytical (exact or manufactured) solutions.
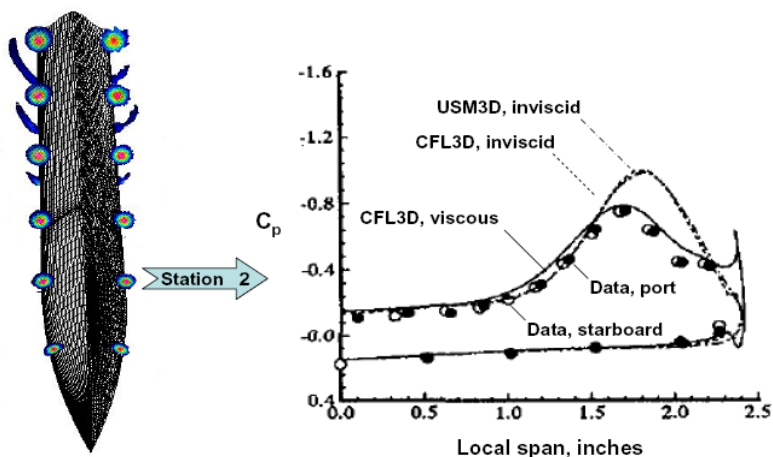
Validation addresses the physics being simulated and how this modeling relates to the real world (often, a physical experiment). However, simple comparisons with experiment have little to do with validation, whereas understanding why a certain simulation matches or misses a certain experiment has very much to do with validation. Put another way, validation involves getting the right answer for the right reason. The numerical answer may match or miss an experimental result depending on how the modelled physics relate to the experimental physics.

Validation motivated research can often involve obtaining sufficient experimental evidence to discriminate how the predictions among various codes and models should relate to the measurements. The work is often conducted on relatively simple shapes which relate to practical aerodynamic topics through the hierarchy described above.

An example of how the right answer may or may not match experiment is shown in **Figure 13** from the vortex flow research of Ghaffari[25] [1994]. The motivation for this work

Figure 13. Correlations among CFD and experiment, MTVI forebody. $M = 0.4$, $R_x = 2.09 \times 10^6$, $\alpha = 19.8^o$. Ghaffari [1994].

was to assess the at-that-time relatively new inviscid/unstructured simulations of sharp-edge vortical flows against what was know from prior structured-grid simulations and experiment. Calculations were performed with the unstructured-grid code USM3D[26] and the structured-grid code CFL3D[27] on the chined forebody of the Modular Transonic Vortex Interaction (MTVI) configuration discussed in Section 3.1.3. Both codes were used to generate inviscid solutions with the Euler equations, and turbulent structured grid solutions from CFL3D were also obtained.

Correlations in Figure 13 are shown at a station where the flow is dominated to a large degree by turbulent flow physics, and the turbulent structured-grid solution from CFL3D correlates fairly well with experiment. To some extent these correlations were expected based upon prior successful application assessments with CFL3D for sharp-edged vortical flows, including but not limited to those by Thomas[27] [1990] for laminar flow about the unit-aspect-ratio delta wing tested by Hummel[6] [1978] and by Ghaffari[28] [1990] for turbulent flow about the F-18 forebody-LEX. Among these results the primary and secondary vortex simulations were shown

to approximate experiment fairly well.

Interpretation of the inviscid (Euler) results requires some additional care. These simulations do not include any secondary-vortex flow physics, and, as discussed in section 3.1.1 of this paper, it is known that diminished secondary vortex effects will result in a more negative primary vortex suction peak that is also further outboard as compared to the viscous condition. The extent of secondary vortex flow was also shown to have little effect on the inboard upper surface pressures and virtually no effect on the lower surface pressures. Both of the inviscid Euler results miss the experiment as they should, and the new unstructured result from USM3D is indistinguishable from the established structured grid result from CFL3D. The Euler simulations miss the experimental results in the manner expected given difference in the flow physics between the two as regards the secondary vortex.

This example of aggregate secondary vortex effects is very simple and by the time of this writing well understood. However, the same care and consideration must be taken for many of the fundamental vortex flow phenomena where the dominant physics are to this day less clear (e.g., vortex breakdown, shock-vortex interactions, blunt leading-edge separation). There is no point adjusting terms in a model that does not represent physics critical to the phenomenology of interest.

4.3 Uncertainty

Validation-motivated experimentation is relatively new and perhaps could not be effectively executed until the fundamental validation concepts[21, 19, 22] matured. In addition, growth of uncertainty principles has contributed yet another critical perspective to validation. Both experimental and numerical uncertainty must be quantified to some extent in order to conduct a validation assessment. Statistical methods are useful to this end, and processes for experimental uncertainty quantification in major wind-tunnel facilities have been developed by Hemsch[29] [2001]. Similar processes have also been reported by Hemsch[30] [2002] for computational uncertainty quantification in association with the drag prediction workshop activities. Although the focus of these works has been toward transonic aerodynamics, the principles are not limited to such, and high-speed perspectives have been reported by Bose[31] [2011] for assessments of aerothermodynamic uncertainties in predictions of hypersonic flight.

The need for uncertainty quantification has necessitated new experimental campaigns to obtain data necessary for validation assessments. Some recent examples include shock/boundary-layer interaction studies as reported by Benek[32] [2010], drag-prediction workshop testing reported by Rivers and Dittberner[33] [2011], and studies of supersonic retropropulsion by Kleb[34] [2011]. As part of the process to quantifying experimental uncertainty these experiments require additional information (e.g., test section flow characterization) than is typically obtained in configuration aerodynamics tests.

Computational uncertainty technologies are also under active assessment and advancement. A Computational Uncertainty Symposium[35] [2007] was recently sponsored by the RTO to help benchmark the numerous methods under development across multiple disciplines. In addition, an application assessment of present methods pertinent to military vehicle interests is being conducted in a new RTO Task Group, AVT 191[36], entitled "Application of Sensitivity Analysis and Uncertainty Quantification to Military Vehicle Design". These activities should be useful for guiding the application of computational uncertainty methods to other problems of interest and are planned to be leveraged toward the current program described next.
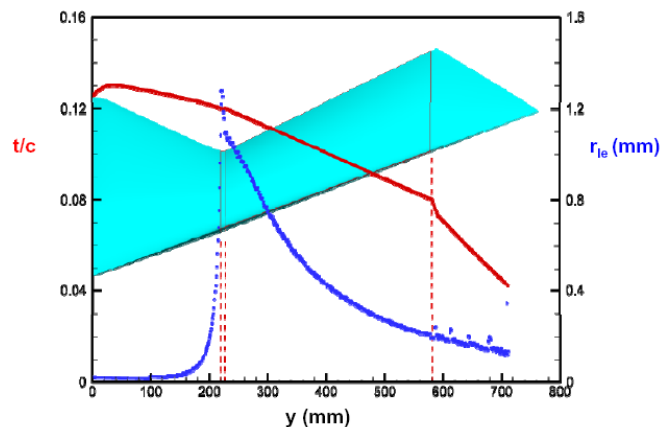
5.0   CURRENT PROGRAM

Development of the new AVT-183 research program is described below. One experiment is being designed, others sought, and a hierarchy of CFD methods is being established to conduct a combined experimental and numerical campaign that is targeted at deficiencies in our understanding of this flow as established by AVT-161 and that will draw on validation and uncertainty principles.

5.1   Parent Problem

The SACCON configuration was designed by EADS and DLR to capture many aspects of UCAV concepts while at the same time being suitable for international collaborative research. The configuration has 53° swept leading and trailing edges. It falls in the semi-slender, lambda-wing class of configurations with a constant chord outer panel and has an aspect ratio of approximately 3.1. The configuration also incorporates fairly complex spanwise distributions of thickness, leading-edge radius, see **Figure 14**, and a linear twist distribution outboard of the first trailing-edge break. The thickness-to-

Figure 14. Some geometric complexities of SACCON.

chord ratio diminishes in the spanwise direction as does the leading-edge radius. In general, the leading-edge radii are less than 0.23% of the SACCON reference chord. The outboard twist delayed separation onset effects to higher angles of attack than would have been realized by a planar wing.

An example of the vortex flow development about the SACCON wing is shown in **Figure 15** with the CFD results of Frink[37] [2010]. At low to moderate angles of attack the attached-flow design objective was achieved. The onset and progression of leading-edge separation however results in an exceptionally complex vortical flow, even for the static conditions of Frink's analysis. Onset is rapid, and the middle angle of attack solution in Figure 15 evidences both an inner vortex, with its origin at the apex of the SACCON wing where the leading edge is sharp, as well as an outer vortex with its origin from the blunt leading edge at about 2/3 wing span. Thus we have a combination of interacting primary vortex flow phenomenology with the onset/progression of blunt leading-edge vortex separation. The region of incipient separation, upstream of the outer vortex separation, is also most curious. Additional analysis has indicated a possible third corotating vortex, slightly inboard of the outer vortex, which forms as part of the blunt leading-edge separation.

With only one degree increase in angle of attack the outer vortex separation progresses up the leading edge to be adjacent to the inner apex vortex. Further increases in angle of attack result in tightly coupled vortex interactions between the co-rotating inner and outer primary vortices and have been interpreted as a source of nonlinear force and moment characteristics for this wing by Frink[37] [2010]. The onset and progression of the blunt leading-edge vortical flow from the outer wing establishes the position and strength of the outer vortex and thus this separation is critical to the vortex interaction aerodynamics. The high angle-of-attack SACCON flow field presents an extremely challenging vortical flow due to simultaneity of vortex interaction effects,
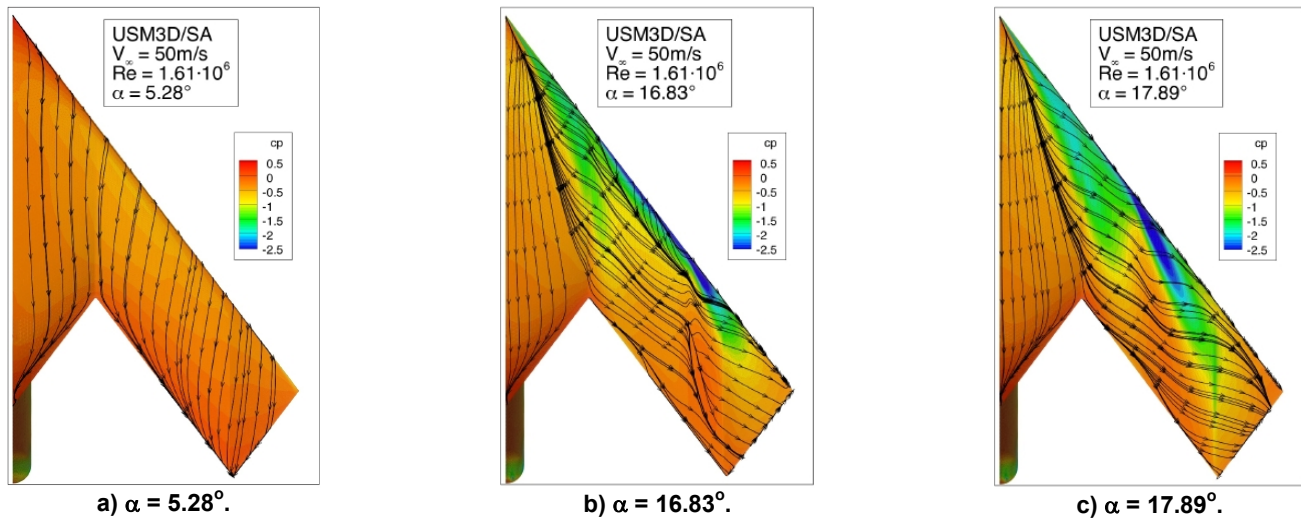
blunt leading-edge separation, and other factors.

| a) α = 5.28°. | b) α = 16.83°. | c) α = 17.89°. |

Figure 15. Complex SACCON vortex flow phenomena. Frink [2010].

5.2   Configuration design

Given the complex nature of the vortical flows about the SACCON configuration, the current program was conceived to isolate one critical aspect of these flows in such a manner to help discriminate why various CFD formulations differ as to their predictive capability (see also section 4.1). The phenomenon chosen was the onset and progression of blunt leading-edge separation on the outboard portion of the wing. The location of the outer vortex is critical to any subsequent vortex interactions with the SACCON apex vortex. The location of the outer vortex separation also fundamentally affects the outer vortex strength and, hence, any manifestations of vortex breakdown.

From a CFD validation perspective, it can be desirable to isolate some of these complex vortical effects in such a manner as to understand why certain methods do or do not predict flows of interest. To this end, the new work under AVT-183 has been spawned to address these details of the blunt leading edge separation in a manner to i) be relevant to the interests of AVT-161, ii) gain information to understand why certain numerical formulation miss or match the leading-edge separation aerodynamics of interest, and iii) seek improved predictive capability.

5.2.1   Conceptual design: geometry/ configuration

The basic approach taken was to keep the new wing as simple as possible while retaining a connection to the flows of interest to SACCON. This would follow the hierarchical approach to code discrimination work described previously in Section 4.1.

A SACCON-relevant unit/benchmark problem was thus conceived based upon a simple diamond wing geometry which could establish the part-span vortical separation. See F**igure 16**. Key aspects of the SACCON leading edge are represented, but the overall wing is greatly simplified. In particular, the leading-edge sweep from SACCON was matched as was the overall magnitude and spanwise trend in leading edge radius for the outer portion of the wing. A constant airfoil section relevant to military applications was also sought, and the initial proposal was for a NACA 64A0xx with thickness to be determined from CFD sensitivity studies. This also results in an initial wing concept with no twist or camber. Apart from keeping the wing as simple as possible, the angle-of-attack loading is a dominant factor for blunt leading-edge separation as reviewed by Polhamus[38] [1996]. In addition, the lack of twist and camber will help generate the desired flow at low to moderate angles of attack where experimental flow quality is better and flowfield measurements can be simpler as compared to high angle-of-attack conditions. Preliminary CFD assessments evidence that the subject blunt leading-edge vortex separation could be created in such a way to facilitate detailed surface and flow-field measurements.
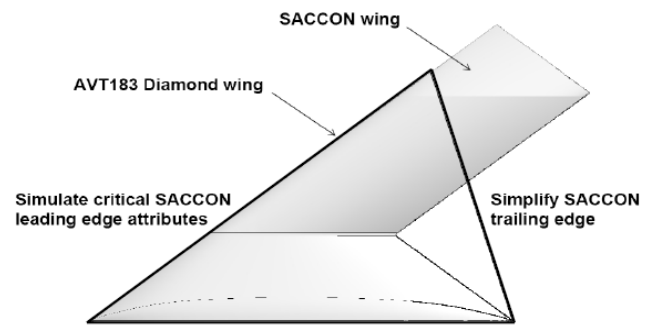
Figure 16. Diamond/SACCON concept. $\Lambda_{le} = 53^o$.

The aerodynamic objective of this design is to isolate, as much as possible, the separation-induced blunt leading-edge vortical flow from the many complexities realized on the SACCON model. The conceptual flow field, and critical measurement regions, are shown in the sketch of **Figure 17**. This would represent the simplest possible vortical flowfield. The sketch shows an isolated blunt leading-edge vortex separation for the notional 53° swept diamond wing, and identifies four flow phenomena and five measurement regions.

The first phenomenon is incipient separation where a better understanding of the separation onset properties is sought. The second phenomenon is the blunt leading-edge vortex and two measurement regions are included. Because of the blunt edge and low sweep, the properties of this vortex will be different from those known in association with the slender sharp-edged delta wing. The third phenomenon is the secondary vortex which, as discussed, affects primary vortex attributes. The primary vortex measurement regions would include measurements of the secondary vortex Finally, the fourth phenomenon is the attached flow on inboard portion of the wing.
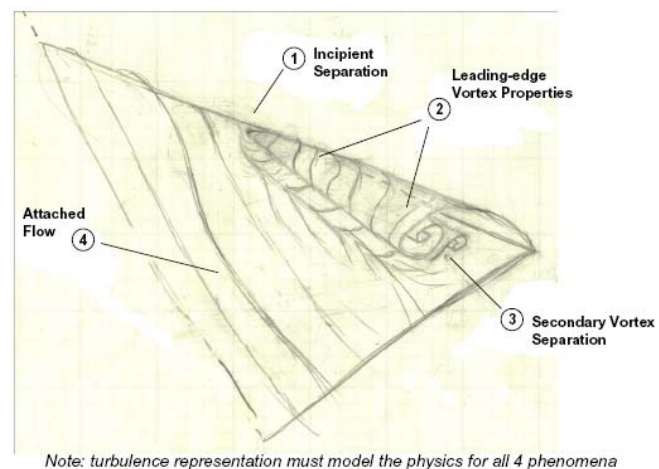
Figure 17. Sketch of flow features.

Although not shown in the sketch, blunt leading-edge vortex separation can also spawn a small, additional inner vortex from the incipient separation region. Much less is known about this vortex, but it represents a possible fifth flow phenomenon and measurements will be performed should it occur. It is observed that any

turbulence model must be able to simulate the flow physics of all these phenomena.

From an experimental perspective it is desirable to fabricate as large a model as is feasible, primarily to facilitate flowfield measurements, and to this end a semispan configuration was selected. Care must be taken with regard to the interface of the model with the wind-tunnel wall/floor, and a peniche (or standoff) was selected as part of the conceptual design. This would result in a simpler geometry, say as compared to a splitter plate, but would also require that the peniche-wall interface flow not interfere significantly with the wing onset and progression of blunt leading-edge separation. This became another factor CFD assessment.

Details of the design were resolved with a rather extensive CFD sensitivity study as described in the following section. During this study the leading-edge sweep was fixed at 53°, being the leading-edge sweep of the SACCON model. The trailing-edge sweep was taken to be 26.5^o, i.e. half of the leading edge sweep. An initial CFD study showed the effect of the trailing-edge sweep to be small.

5.2.2   CFD sensitivity assessments

Primary configuration parametric trends were assessed with the block-structured RANS code ENSOLV which is part of the simulation system ENFLOW[39] from the NLR. A smaller number of assessments were performed with the unstructured RANS code USM3D[26] from NASA LaRC. Selected results from the work follow.

5.2.2.1 Thickness/leading-edge radius, angle of attack.

An extensive CFD sensitivity assessment study was conducted to help guide the configuration definition of the subject investigation. These studies first focussed on combined thickness/leading-edge-radius effects, per the 64A0xx class of airfoils, on the sought leading-edge separation phenomenology.

Three profiles, a NACA 64A0010, NACA 64A008 and NACA 64A006, were used. See **Figure 18.** These profiles have leading-edge radii, in percent chord, of 0.687, 0.439, and 0.246 respectively. The trailing edge of these profiles was closed by replacing the last one percent of the chord by a quadratic curve.

Figure 18. Sketch of NACA64A0xx profiles.

Based on these profiles a diamond wing with a root chord of one meter was constructed. The leading-edge sweep and trailing-edge sweep of this diamond wing configuration were 53° and 26.5^o, respectively.
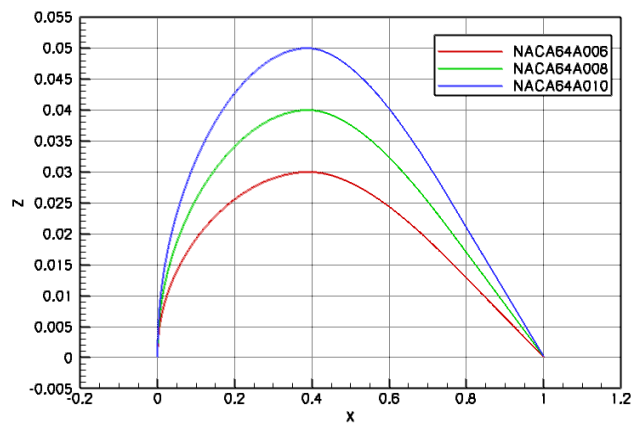
Next a structured multi-block grid, consisting of 56 blocks and about 3 million grid cells, was generated around the diamond wing using NLR's in-house grid generation tools. Though being relatively coarse, this grid was judged sufficient to obtain a first estimate of the separation behaviour of the different wings.

For all three wings, an angle-of-attack sweep was performed at nominal target condition, i.e. a Mach number M of 0.2 and a Reynolds number based on the mean aerodynamic chord, R_{mac}, of 3 x 10^6. Angles of attack

between 0° and 20° were simulated at a 1° interval. These simulations were performed using the NLR flow solver ENSOLV. They were run in fully turbulent mode employing the TNT k-ω turbulence model. With regard to convergence, 1500 number of cycles were typically sufficient to produce a 3 order drop of residuals.

Figure 19 compares the results obtained at an angle of attack of 12°. The results in this figure, as well as similar figures that follow, are displayed with surface contours of the static pressure coefficient and off-body

a) NACA 64A010   **b) NACA 64A080**   **c) NACA 64A006**
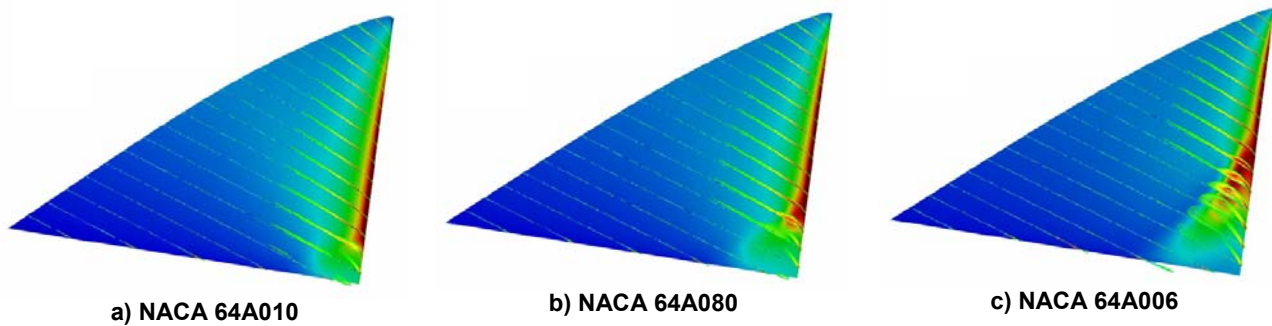
Figure 19. CFD assessment for NACA 64A0xx diamond wing. ENSOLV, TNT k-ω, M = 0.2,
R_{mac} = 3 x 10^6, α=12°.

contours of the x-component of vorticity. These simulations showed that at an angle of attack of 12° (which is approximately the target angle of attack for the wind tunnel experiments) only the NACA64A006 exhibits the desired flow separation at about half way the wing leading edge. This airfoil has the closest leading edge radius (r_{le}/c = 0.246%) to corresponding values for the outboard portion of the SACCON wing ($r_{le}/cref$ < 0.23%).

Angle of attack effects for the diamond wing with the NACA 64A006 airfoil are shown in **Figure 20** for several angles of attack at the nominal target flow conditions, M = 0.2 and R_{mac} = 3 x 10^6. The results show


a) α=8°   **b) α=10°**   **c) α=12°**
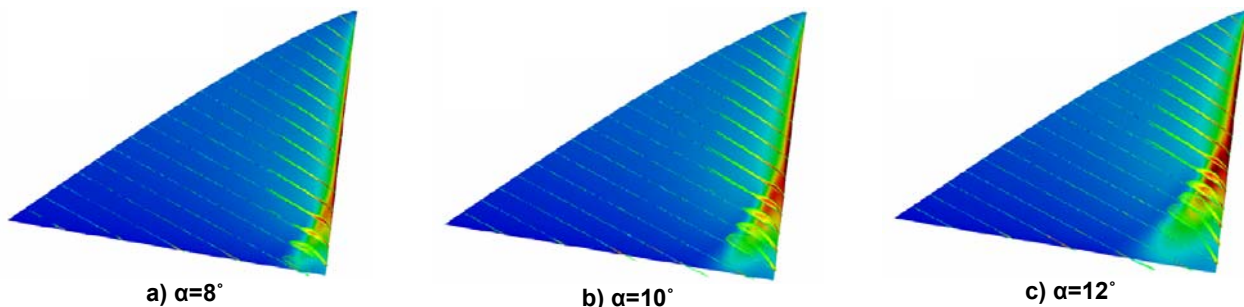
Figure 20. CFD assessment for NACA 64A006 diamond wing. ENSOLV, TNT k-ω, M = 0.2,
R_{mac} = 3 x 10^6.

that the desired flow phenomenon, the onset and progression of blunt leading-edge vortical separation, has been achieved. In addition the results show a fairly smooth progression of this separation with angle of attack. This smooth progression is very desirable from an experimental perspective.

Grid sensitivity analysis was also performed. The grid dimensions in all directions were mutlitplied by 1.5, and the resulting grid consisted of 10.2 million grid points. Both results on the original and fine grid are shown in **Figure 21**.

Though the surface pressure coefficient on the fine mesh shows a higher pressure peak underneath the vortex and also a some more detailed signature, the separation location is approximately the same (halfway along the wing leading edge)

a) 3 million grid cells   b) 10.2 million grid cells
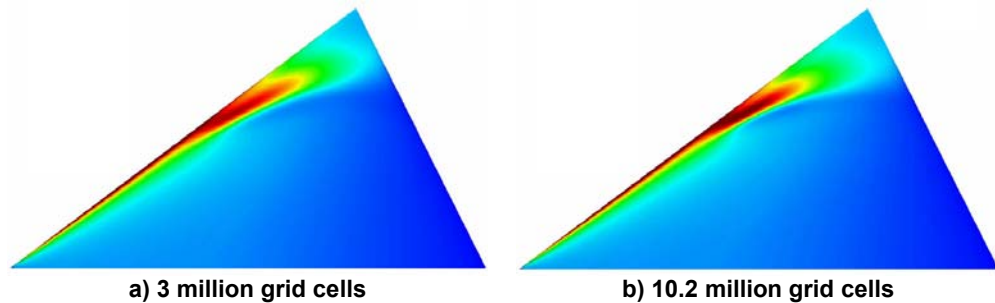
Figure 21. Grid sensitivity for NACA 64A006 diamond wing. ENSOLV, TNT k-ω, M = 0.2, R_{mac} = 3 x 10^6, α = 12˚.

The results of these investigations led to the selection of a NACA 64A006 airfoil with a diamond wing planform that matched the SACCON leading-edge sweep angle (53˚) and had half that value for the trailing-edge sweep angle (26.5˚).

5.2.2.2 Independent numerical check, isolated thickness and ler effects, turbulence model effects

A smaller number of independent computations were performed with the unstructured RANS solver USM3D. The calculations were focused in the nominal target condition (M = 0.2, R_{mac} = 3 x 10^6, α = 12°) and included i) a comparison between the structured grid and the unstructured grid results, ii) an assessment to isolate thickness and leading-edge radius effects on the blunt leading-edge separation, and iii) an assessment of turbulence model sensitivities. Angle of attack effects were computed with the unstructured method for the NACA 64A006 diamond wing, and these results showed very similar results of onset and progression for leading-edge vortex separation that were obtained from the structured grid results as shown in section 5.2.2.1.

NACA 64Axxx airfoil leading-edge radius and thickness are coupled, so results shown in Figure 19 include effects of both. A hybrid airfoil was designed with the leading-edge radius of the NACA 64A006 and the thickness of the NACA 64A010 while retaining the overall class of pressure distribution of the NACA 64Axxx airfoil class. An unstructured-grid calculation at α = 12° showed basically similar results to NACA 64A006 unstructured results as well as the structured-grid results shown in Figure 19. This limited result implies that leading-edge
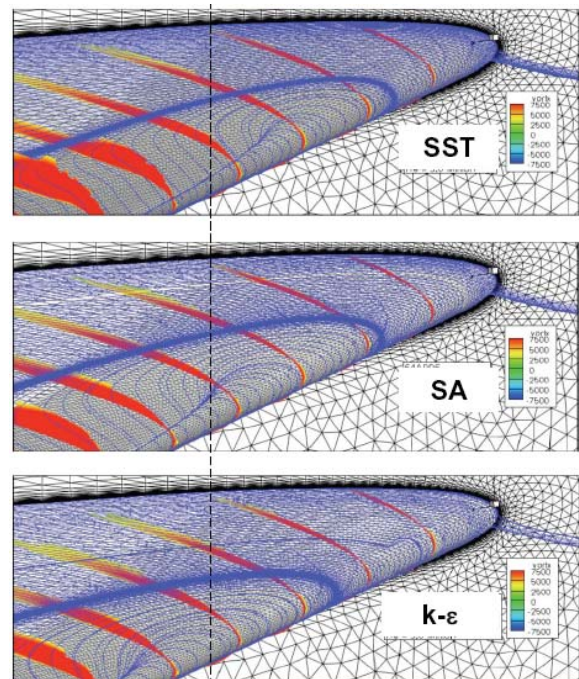
Figure 22. Turbulence model assessment for NACA 64A006 diamond wing. USM3D, M = 0.2, R_{mac} = 3 x 10^6, α = 12°.

radius is affecting the blunt leading vortical separation for this diamond wing to a greater degree than airfoil thickness.

Finally, three turbulence models (SA, SST, k-ε) were used with the unstructured method to assess their effect on the blunt leading-edge separation for the diamond wing at the nominal target condition (M = 0.2, R_{mac} = 3 x 10^6, α = 12°). This study demonstrated a significant shift in separation onset location around a point halfway along the wing leading edge, and the results are shown in **Figure 22**. In this figure, the shift in separation onset due to turbulence model is approximately 16% of leading-of the distance down the edge. This result demonstrates the need for experimental data which will enable improved turbulence models so that a more consistent solution for the separation onset location and resulting separation will be obtained.

5.2.2.3 Wind tunnel model related assessments

Additional simulations were performed for the wind tunnel model (c_r = 1.2m) with the blocked-structured solver ENSOLV. These simulations include the effects of a planned peniche (h = 0.090m = 0.075 c_r) and wind-tunnel floor boundary layers (entrance length of 2c_r = 2.4m) to integrate the model with the wind tunnel environment. This entrance length was sufficient to approximate the floor boundary layer thickness. The grid consisted of 134 blocks and 13.5 million grid cells. Simulations were performed for the expected wind tunnel conditions, i.e. a Mach number M of 0.15 and a Reynolds number R_{mac} of 2.7 million. These simulations were run in fully turbulent mode employing the EARSM turbulence model

a) α = 10° b) α = 12° c) α = 14°
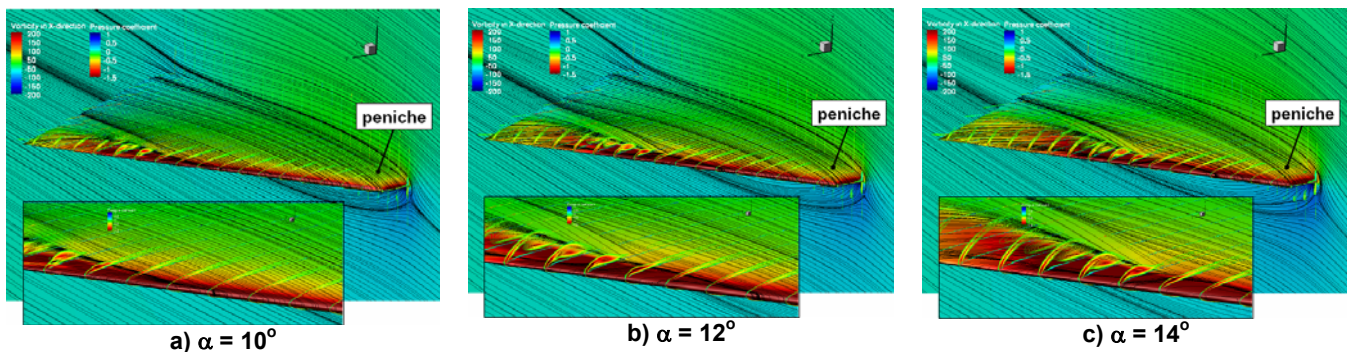
Figure 23. CFD assessment for NACA64A006 diamond wing (c_r = 1.2m) including peniche (h = 0.090m = 0.075 c_r). ENSOLV, EARSM, M = 0.15, R_{mac} = 2.7 x 10^6

Angle of attack sensitivities for this geometry are shown in **Figure 23**. These results demonstrate once more a smooth progression of the leading-edge separation with angle of attack. In addition, they show that the horse shoe vortex at the wall/peniche intersection is only limited to a small region and thus does not significantly influence the flow over the wing.

5.3   Experimental program considerations

Based on the above CFD study a wind tunnel model has been designed and is ready for fabrication. Details of the wind tunnel model and planned testing are described in the following sections.

5.3.1 Model

A semi-span wind tunnel model has been designed for testing at the Technical University, Munich. As indicated before, the wind tunnel model will have a diamond wing planform with a root chord of $c_r = 1.2$m. The leading-edge and trailing-edge sweep are 53° and 26.5^o, respectively. The wind tunnel model has a constant airfoil section, being the NACA 64A006 profile.

The overall dimensions of the model have been chosen such that the model is as large as possible to enable high-quality/high-resolution measurements (especially near the leading edge) while not incurring unacceptable wall interference effects. This size also falls within fabrication and budget constrains and could enable testing in other facilities.

The complete model (including the peniche) is shown in **Figure 24**. The model will consist of the following parts:

- Lower and upper surface plate (gray),
- Wing tip section (red),
- Leading-edge section (blue, consisting of two parts),
- Trailing-edge section (green, consisting of two parts),
- Leading-edge inserts for pressure ports (gray),
- Peniche (h = $0.075c_r$ = 0.090m); the gap between the wing and peniche will be sealed with a labyrinth seal., and
- Balance adapter.
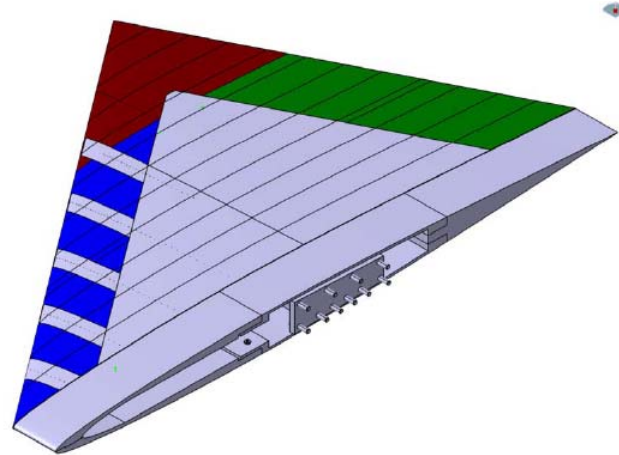
Figure 24. Wind tunnel model (including peniche).

The model will be fabricated out of aluminium (CERTAL). This material will result in a very stiff model for the anticipated loads. It is noted that the wing leading edge will have to be fabricated in two parts. This had to be done due to machining constraints for the length of inboard segment and due to machining and loads considerations for the very thin wing tip. It is anticipated that the model material will support development of a high-quality surfaces such that final finishing should remove effects due to the seam between these parts. The model fabrication is being planned to start late in 2011 and to be finished in the middle of 2012.

5.3.2 Testing

Tests are being planned for the low-speed tunnel at the Technical University, Munich. This wind tunnel has a test section area of 1.80m x 2.40m, and a test section length of 4.80m. During the experiments the wind tunnel will be run in open section mode to facilitate flowfield measurements. The maximum speed in the open test section mode is 65m/s.

The wing measurements are being planned to include:

- Force and moment measurements using an external six-component balance,

- model vibrations,

- Static surface pressure measurements,

- Unsteady surface pressure measurements, and

- Velocity measurements using both hot-wire anemometry (HWA) and particle image velocity (Stereo PIV). These will be performed at overlapping regions such that they provide complementary information for velocity fields and measurement device effects.

A more limited set of measurements on the peniche and neighbouring wind tunnel floor are also being planned.

The wind tunnel tests at the Technical University, Munich are planned for the middle of 2012, and details for these experiments are being developed. Interest has also been voiced to perform experiments at other institutions, and the possibility of such experiments using the model of the Technical University Munich will be investigated.

5.4   CFD program considerations

In addition to the wind-tunnel program an extensive CFD program has been initiated. To a large degree, the preliminary phase of the CFD program has been described in this paper. Subsequent phases will include pre-test activities, post-test activities, and prediction assessments. It is intended to broaden the suite of numerical methods for these phases to include RANS, URANS, LES, and DES techniques.

5.4.1 Pre- and Post-test activities

The pre-test phase will be blind-test predictions for the anticipated data. These are planned for the periods leading up to and during the execution of the experiment. Comparisons among the CFD results prior to experiment could help guide decisions for data acquisition. Current best practices can also be baselined as they apply to the target flow.

The post test phase will focus on assessments against the new experimental data. Beyond simple comparisons between experiments and numerics, this phase will seek to identify why the different solutions match or miss the critical flow separation effects (c.f., section 5.4). Both the experimental and numerical data will be scrutinized for enhanced understanding of blunt leading edge separation and the subsequent vortical phenomena. Numerical results will need to be dissected with regard to matters such as the properties of the specific turbulence models used, grid resolution requirements, specific solver settings such as low Mach-number preconditioning, and cross-solver physics-based modelling effects (e.g., RANS vs. URANS, URANS vs. LES, etc.).

5.4.2   Modeling assessments and improvements

To the extent that CFD modeling is altered, assessments are being considered in three tiers. See **Figure 25**. The first tier is self-assessment against the data used for the model improvement. Such assessments are necessary for model evaluation, but they are not sufficient for any predictive capability assessment. The second tier constitutes a primary predictive assessment where models developed from the diamond wing campaign are applied to the (parent) SACCON configuration at relevant conditions to assess predictive improvements. The third tier constitutes secondary assessments against other relevant configurations. Plans for these will include a related UCAV concept[40], recent RTO sponsored work[41], and selected data sets from literature[42, 43, 44]. Overall recommendations for revised best practices, modelling improvements, or even modelling abandonment will be sought.
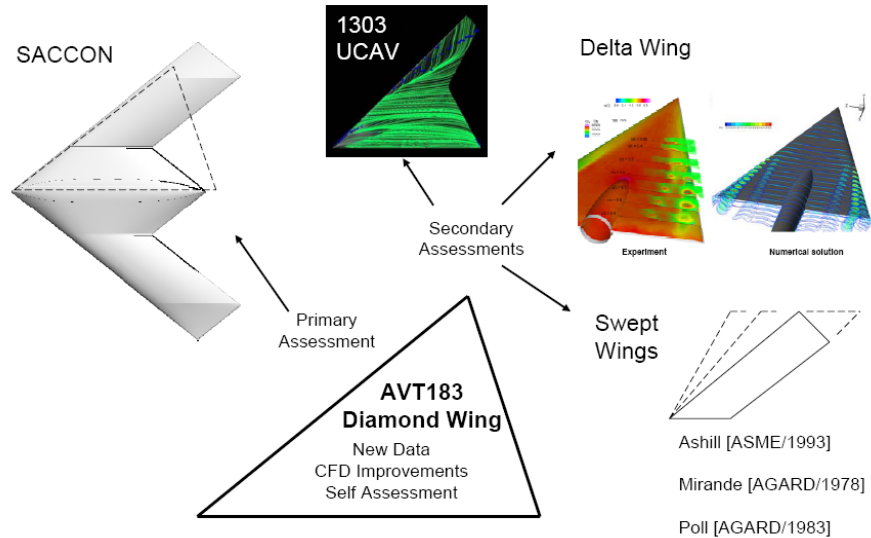
Figure 25. Computational assessments for predictive capability.

6.0   CONCLUDING REMARKS

Uninhabited Combat Air Vehicles present many aerodynamic prediction challenges, and the recent RTO Task Group AVT-161, entitled "Assessment of Stability and Control Prediction Methods for NATO Air & Sea Vehicles", has provided some significant progress toward these predictions with an emphasis on dynamic stability. In addition, this task group has identified challenge remaining for further research. A new RTO Task Group, AVT-183 entitled "Reliable Prediction of Separated Flow Onset and Progression for Air and Sea Vehicles", has been formed to address some of the challenges from AVT-161. This paper has presented an overview of the AVT-183 research program, both in terms of technical content and in terms of the relationship between these two task groups.

Task Group AVT-161 demonstrated deficiencies in our understanding of the blunt leading-edge vortex separation for a UCAV configuration known as SACCON. The SACCON flowfields were found to be very complex and included many interacting vortical flows. For AVT-183, a reduced-complexity investigation of blunt leading-edge vortex separation was created in such a manner as to (i) be relevant to the interests of AVT-161, (ii) isolate blunt leading-edge vortex separation for experimental and numerical assessment, and (iii) seek improvements for CFD predictive capability.

The AVT-183 research will focus on a diamond wing with a constant airfoil section. Preliminary CFD

assessments have demonstrated that the subject blunt leading-edge vortex separation can be created with this simple shape, and details to arrive at this reduced complexity project have been described. The future work will include both experimental and numerical investigations intended to help distinguish modeling requirements for successful prediction of blunt leading-edge vortex separation relevant to UCAV aerodynamics.

7.0 ACKNOWLEDGEMENT

8.0   REFERENCES

[1]   Luckring JM. A Survey of Factors Affecting Blunt Leading-Edge Separation for Swept and Semi-Slender Wings. AIAA 2010-4820, Jun 2010.

[2]   Cummings RM, and Schütte A. An Integrated Computational/Experimental Approach to UCAV Stability & Control Estimation: Overview of NATO RTO AVT- 161. AIAA 2010-4392, Jun 2010.

[3]   Frink NT, Tormalm M, and Schmidt S. Unstructured CFD Aerodynamic Analysis of a Generic UCAV Configuration. RTO-MP-AVT-189, Paper 25, Nov 2011.

[4]   Schütte A, Hummel D, and Hitzel SM. Numerical and Experimental Analyses of the Vortical Flow Around the SACCON Configuration. AIAA 2010-4690, Jun 2010.

[5]   Thacker BH, Francis WL, and Nicolella DP. Model Validation and Uncertainty Quantification Applied to Cervical Spine Injury Assessment. RTO MP-AVT-147, Paper 26, Dec 2008.

[6]   Hummel D. On the Vortex Formation Over a Slender Wing at Large Incidence. *AGARD CP-247*, Paper 15, Jan 1979.

[7]   Hummel D. Effects of Boundary Layer Formation on the Vortical Flow above Slender Delta Wings. RTO MP-AVT-111, Paper 30, Oct 2004.

[8]   Smith JHB. Improved calculations of leading-edge separation from slender delta wings. RAE TR 66070, 1966.

[9]   Lambourne NC, and Bryer DW. The Bursting of Leading Edge Vortices - Some Observations and Discussion of the Phenomenon. ARC R&M 3282, 1962.

[10]   RTO. Vortex Breakdown over Slender Delta Wings. RTO-TR-AVT-080, Oct 2009.

[11]   Mitchell AM. Experimental Data Base Selected for RTO/AVT Numerical and Analytical Validation and

Verification: ONERA 70-Deg Delta Wing. AIAA Paper 2003-3941, Jun 2003. See also Chapter 3, RTO-TR-AVT-080, Oct 2009.

[12] Hall RM. Impact of Fuselage Cross Section on the Stability of a Generic Fighter. AIAA 1998-2725, Jun, 1998.

[13] Schiavetta LA, Boelens OJ, Crippa S, Cummings RM, Fritz W, and Badcock KL. Shock Effects on Delta Wing Vortex Breakdown. AIAA Journal of Aircraft, Vol. 46, No. 3, May-Jun 2009.

[14] Miller DS, and Wood RM. Lee-Side Flow Over Delta Wings at Supersonic Speeds. NASA TP 2430, Jun 1985.

[15] Stanbrook A, and Squire LC. Possible Types of Flow at Swept Leading Edges. Aeronautical Quarterly, Vol. XV, pt. 1, Feb 1964.

[16] Luckring JM. Reynolds Number, Compressibility, and Leading-Edge Bluntness Effects on Delta Wing Aerodynamics. ICAS 04-414, Sep 2004.

[17] Konrath R, Klein C, and Schroeder A. PSP and PIV Investigations on the VFE-2 Configuration in Sub- and Transonic Flow. AIAA 2008-379, Jan 2008.

[18] Hemsch MJ, and Luckring JM. Connection Between Leading-Edge Sweep, Vortex Lift, and Vortex Strength for Delta Wings. AIAA Journal of Aircraft, Vol. 27, No. 5, May 1990.

[19] ASME. Guide for Verification and Validation in Computational Solid Mechanics. ASME V&V 10-2006, Dec 2006

[20] Wilson GE, and Boyack BE. The role of the PIRT process in experiments, code development and code applications associated with reactor safety analysis. Nuclear Engineering and Design, Vol. 186, 1998.

[21] AIAA. Guide for the Verification and Validation of Computational Fluid Dynamics Simulations. AIAA G-077-1998, Jan 1998

[22] ASME. Standard for Verification and Validation in Computational Fluid Dynamics and Heat Transfer. ASME V&V 20-2009, Nov 2009

[23] Oberkampf WL, and Trucano TG. Verification and Validation in Computational Fluid Dynamics. Progress in Aerospace Sciences, Vol. 38, 2002

[24] Oberkampf WL, and Roy CJ. Verification and Validation in Scientific Computing. Cambridge University Press, 2010.

[25] Ghaffari F. On the Vortical-Flow Prediction Capability of an Unstructured-Grid Euler Solver. AIAA 94-0163, Jan 1994.

[26] Frink NT. Upwind Scheme for Solving the Euler Equations on Unstructured Tetrahedral Meshes, AIAA Journal, Vol. 30, No. 1, 1992.

[27] Thomas JL, Krist SK, and Anderson WK. Navier-Stokes Computations of Vortical Flows Over Low

Aspect Ratio Wings. AIAA Journal, Vol. 28, No. 2, Feb 1990.

[28] Ghaffari FG, Luckring JM, Thomas JT, and Bates BL. Navier-Stokes Solutions About the F/A-18 Forebody-Leading-Edge Extension Configuration. AIAA Journal of Aircraft, Vol. 27, No. 9, Sep 1990.

[29] Hemsch MJ, Grub J, Krieger W, and Cler D. Langley Wind Tunnel Data Quality Assurance - Check Standard Results. AIAA 2000-2201, Jun 2001.

[30] Hemsch MJ. Statistical Analysis of CFD Solutions from the Drag Prediction Workshop. AIAA 2002-0842, Jan 2002.

[31] Bose D, Brown JL, Prabhu DK, Gnoffo P, Johnston CO, and Hollis B. Uncertainty Assessment of Hypersonic Aerothermodynamics Prediction Capability. AIAA 2011-3141, Jun 2011.

[32] Benek JA. Lessons Learned from the 2010 AIAA Shock Boundary Layer Interaction Prediction Workshop. AIAA 2010-4825, Jun 2010.

[33] Rivers MB, and Dittberner A. Experimental Investigations of the NASA Common Research Model in the NASA Langley National Transonic Facility and NASA Ames 11-Ft Transonic Wind Tunnel. AIAA 2011-1126, Jan 2011.

[34] Kleb WL, Schauerhamer DG, Trumble K, Sozer E, Barnhardt M, Carlson J, and Edquist K. Toward Supersonic Retropropulsion CFD Validation. AIAA 2011-3490, Jun 2011.

[35] RTO. Computational Uncertainty. RTO-MP-AVT-147, Dec 2007.

[36] RTO. Application of Sensitivity Analysis and Uncertainty Quantification to Military Vehicle Design. RTO Task Group AVT-191.

[37] Frink NT. Strategy for Dynamic CFD Simulations on SACCON Configuration. AIAA 2010-4559, Jun 2010.

[38] Polhamus EC. A Survey of Reynolds Number and Wing Geometry Effects on Lift Characteristics in the Low Speed Stall Region. NASA CR-4745, Jun 1996.

[39] Boerstoel JW, Kassies A, Kok JC, and Spekreijse SP. ENFLOW, a Full-Functionality System of CFD Codes for Industrial Euler/Navier-Stokes Flow Computations. NLR TP 96286U, NLR, Amsterdam, 1996.

[40] Petterson K. CFD Analysis of the Low-Speed Aerodynamic Characteristics of a UCAV. AIAA 2006-1259, Jan 2006.

[41] RTO. Understanding and Modeling Vortical Flows to Improve the Technology readiness Level for Military Aircraft. RTO-TR-AVT-113, Oct 2009.

[42] Ashill PR, and Betts CJ. A Study of the Flow around the Leading Edge of a Highly-Swept Wing in a Low-Speed Wind Tunnel. ASME Engineering Conference, Jun 1993

[43] Mirande J, Schmitt V, and Werle H. Vortex Pattern Developing on the Upper Surface of a Swept Wing

at High Angle of Attack. AGARD CP 247, Paper 12, Jan 1979.

[44] Poll DIA. On the Generation and Subsequent Development of Spiral Vortex Flow Over a Swept-Back Wing. AGARD CP-342, Paper 6, Jul 1983.